PHYSICAL REVIEW B **68**, 214101 (2003)

Atomic-scale model of the grain boundary potential in perovskite oxides

R. F. Klie,* M. Beleggia, and Y. Zhu
Department of Materials Science, Brookhaven National Laboratory, Upton, New York 11973, USA

J. P. Buban
Department of Physics, University of Illinois at Chicago, Chicago, Illinois 60607, USA

N. D. Browning
Department of Chemical Engineering and Materials Science, University of California-Davis, Davis, California 95616, USA

(Received 27 June 2003; published 9 December 2003)

A combination of experiments and theoretical calculations is used to develop an atomic-scale model of the grain boundary potential in perovskite oxides. More specifically, pristine 8° and 58° [001] tilt grain boundaries in $SrTiO_3$, which can be regarded as model systems for all cubic perovskite systems, are examined by Z-contrast imaging and electron-energy-loss spectroscopy. Based on results obtained from these systems, distance-valence least-square analysis and multiple-scattering calculations are used to determine the density of grain boundary states for the 8° and 58° grain boundaries, respectively. To compute the grain boundary potentials, the Thomas-Fermi approach of screened charges and the classical Schottky model is used. The validity of both models for various perovskite oxide grain boundary configurations is discussed, and the appropriate grain boundary potentials are compared with previously reported data.

DOI: 10.1103/PhysRevB.68.214101 PACS number(s): 61.72.Mm, 68.37.Lp, 71.22.+i, 82.80.Pv

INTRODUCTION

Polycrystalline perovskite oxides exhibit a wide variety of properties, such as ferroelectricity, mixed conductivity, and high-T_c superconductivity.[1–3] Many of these properties are heavily influenced by the presence and behavior of internal interfaces. The cubic perovskite $SrTiO_3$ is often regarded as a model system for more complex perovskite oxide grain boundaries,[4–6] where the bulk properties are very well understood from defect chemistry principles. $SrTiO_3$ itself has application as positive thermal coefficient thermistors, piezoactuators, boundary layer capacitors, and varistors due to its limited rate of transport of matter and charge through boundaries and enhanced transport along boundaries, all of which are highly important for the overall device response. Therefore to develop a fundamental understanding of the structure-property relationships at grain boundaries in perovskites, much can be inferred from the study of the $SrTiO_3$ model system.

While the bulk of simple cubic perovskite oxides is well understood, there is still considerable debate as to the origin of many widely observed grain boundary properties. Many theories introduce generic grain boundary states to explain the microscopic properties of grain boundaries that lead to the formation of a double Schottky barrier.[7] In these models, the boundary states are induced by the presence of a two-dimensional (2D) sheet of immobile charges in the grain boundary plane, which are compensated by an opposite space charge in a depletion layer on either side of the boundary.[7] While this model assumes a homogeneous distribution of these grain boundary states, which is strictly only true for high-angle interfaces where the grain boundary dislocation cores overlap, it cannot account for local variations in the density of grain boundary states. In addition, this model assumes that in the area close to the dislocation cores, all charge carriers are completely depleted up to the width of the depletion layer. The Schottky model is therefore unsuitable for low-angle interfaces in materials with a screening length of less than 4 nm.

The Thomas-Fermi screening model presents an alternative approach for describing the interfacial potentials in perovskite oxides. The validity of the Thomas-Fermi screening approach relies on a certain number of assumptions. In particular, to establish the Thomas-Fermi equation, it is required that the solution (i.e., the electrostatic potential) is a perturbation with respect to the Fermi level of the material. Moreover, the dielectric response of the material is considered as a rough approximation, not including the quantum effects described in the Linnard-Jones approach.[8] These will appear if the inverse screening length of the material is of the same order as the Fermi wave vector. Finally, the edges of the band responsible for the conduction should be sufficiently far away from the Fermi level in order to provide enough carriers for the screening.

When these assumptions are not satisfied, for example, with a Fermi level very close to the band top or bottom edge, or for very large total potentials, the Thomas-Fermi screening model requires a generalization which leads to the semiconducting-type approach. It is important to point out that the classical Schottky approach, which is suitable to describe the screening after the band has been completely depleted or filled (i.e., the Fermi level crosses one of the band edges), is *not* easily generalized in the region where the Thomas-Fermi approach is valid. The two descriptions are thus complementary, and particular care has to be taken in order to establish which description is suitable for the system under investigation.

Several high-resolution transmission electron microscope studies and microanalysis results have suggested amorphous phases or cation interstitials to be the origin of the charge

©2003 The American Physical Society

imbalance in the boundary plane.[9,10] The width of the space-charge layer, correlated to the grain boundary potential, was determined by energy dispersive spectroscopy mapping,[10] impedance spectroscopy,[11,12] and electrochemical measurements. The effective width of the grain boundary depletion layer in acceptor doped $SrTiO_3$ ceramics has been determined to be 30 nm–200 nm, decreasing with increasing acceptor concentration.[4] However, none of these techniques is capable of performing the experiments with the needed accuracy and spatial resolution to measure the grain boundary width.

More recently, the correlation between the structural and the local electronic properties of $SrTiO_3$ grain boundaries was obtained by the combination of Z-contrast imaging and electron-energy-loss spectroscopy (EELS) in the scanning transmission electron microscope (STEM).[5,6,13,14] In these studies it was found that [001] tilt grain boundaries contain characteristic sequences of structural units that do not contain any intergranular grain boundary phases.[5] However, these structural units did contain reconstructions that were proposed to give rise to the local states responsible for the electronic behavior of the grain boundary.[6] Self-consistent *ab initio* density-functional calculations of these units now suggest that the behavior is subtler than previously proposed. In particular, it has been shown that it is energetically favorable for there to be an excess of oxygen vacancies in these units, and in the case of units centered on the Ti sublattice, a Ti excess.[15] Such nonstoichiometry leads to the formation of a highly donor doped, or *n*-type region, at the boundary rather than the formation of a Schottky barrier.

In this paper, we will show direct experimental evidence for the presence of the proposed excess of oxygen vacancies in the grain boundary plane that is independent of the cation arrangement, and we will develop an atomic-scale model of the grain boundary potential for undoped tilt grain boundaries in perovskite oxides that can be easily extrapolated to a variety of acceptor doping concentrations and grain boundary misorientation angles. The concentration profile of excess charges in the grain boundary is measured by column-by-column EELS for each dislocation core. Based on these measurements, we developed two different interfacial charge distributions. The first one describes the charge carriers as a series of individual dislocation core charges in the grain boundary plane [see Fig. 1(a)]. Whether these individual core charges overlap is solely determined by the spacing between the dislocations and the width of the core charges [see Fig. 1(b)]. The transition from a low-angle grain boundary, where the interfacial charge profiles per structural unit do not overlap, to a high-angle interface occurs in $SrTiO_3$ at $\sim 14°$. The second charge distribution utilizes a 2D wall of charges located at the grain boundary plane. For both experimental results, the low-angle as well as the high-angle grain boundary, we will use the Thomas-Fermi screening and the Schottky approach to calculate the interfacial potentials and evaluate the validity of the different models for each individual case. We will conclude by showing that an atomic-scale model of interfacial potentials can explain the values previously reported in the literature for both, the low- and high-angle grain boundary potentials.

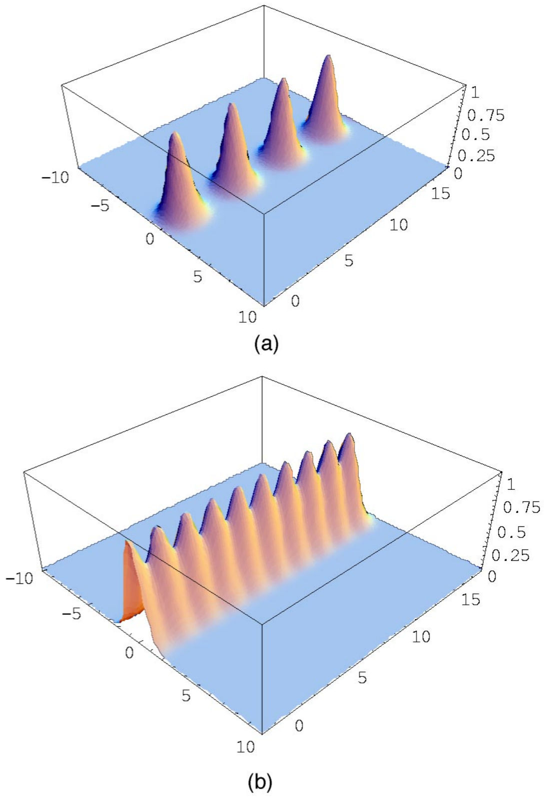

FIG. 1. 3D view of the charge distribution of dislocation cores (a) for a low-angle and (b) for a high-angle grain boundary.

EXPERIMENTAL SETUP

The results that are presented in this paper are obtained using the JEOL 3000F and the JEOL 2010F transmission electron microscopes (TEM); the EELS results were obtained using the JEOL 2010F. Both microscopes are equipped with an ultra highresolution objective lens pole piece, a JEOL annular dark-field detector, a postcolumn Gatan imaging filter, and a NORAN x-ray detector. The instruments are capable of being operated in either the conventional TEM or scanning TEM mode. For the atomic resolution imaging and analysis results shown here, the incoherent high-angle annular dark-field imaging mode in STEM was used exclusively. The key to atomic resolution in STEM[16–18] is the formation of the smallest possible electron probe with sufficient probe current (40 pA) to obtain statistically significant images and spectra. The electron probe is optimized using the electron ''Ronchigram,'' or ''shadow image'' (for a more detailed description see Refs. 16 and 19), to obtain a probe size of ~ 0.2 nm for these experiments.

The experimental setup of this microscope allows using the low-angle scattered electrons that do not contribute to the *Z*-contrast image for EELS.[20] As the two techniques do not interfere, this means that *Z*-contrast images can be used to position the electron probe at the desired spot in the sample and to acquire spectra.[16,21,22] The physical principle behind EELS relates to the interaction of the fast electrons with the sample to cause either collective excitations of electrons in the conduction bands (plasmons), or discrete transitions between atomic energy levels.[20]

For perovskite oxides, we are primarily interested in the bonding between oxygen and the transition-metal atoms. To investigate this, the near-edge fine structure of the oxygen *K* edge contains valuable information about the nearest-neighbor bonding (O $2p$ with metallic $3d$) and the hybridization with the metal sp band.[6] For example, the titanium core-electron transitions from $2p^63d^m$ to $2p^53d^{m+1}$, which indicate the number of available orbitals for hybridization with the oxygen bands, lie in the sensitive part of the energy-loss spectrum.

The formal valence state of the transition-metal elements in the structure can be determined from the analysis of the L_2 and L_3 white lines that are visible due to the spin-orbit interaction. More specifically, the L_3 and L_2 lines are a result of the transitions $2p^{3/2}\rightarrow 3d^{3/2}3d^{5/2}$ and $2p^{1/2}\rightarrow 3d^{3/2}$, respectively. Further, the chemical shift of the transition metal L-edge onset can be correlated directly to its formal oxidation state. However, the theoretical calculation of the absolute L_3/L_2 ratio or the absolute edge-onset energy still requires substantial improvement. Hence, the experimental values for an unknown transition-metal oxidation state must be compared either with results from the literature or parametric fits calculated from structures with well-known oxidation states, to convert the measured intensities and edge onset into numerical ionization values.

RESULTS

8° [001] tilt grain boundary

Figure 2(a) shows a *Z*-contrast image of an 8° [001] tilt grain boundary in $SrTiO_3$ in the (001) orientation. The micrograph contains the two adjacent grains with cubic symmetry (space group: P_{m3m}, $c=3.9$ Å) and five dislocation cores at the grain boundary, which show up as dark ovals due to the stress surrounding the dislocation core. The spacing between the cores was determined to be (26.8 ± 0.7) Å, and the misorientation angle was measured at $(8.3\pm0.2)°$. Figure 2(b) shows a higher magnification image of one of the dislocation cores. The brighter columns in the bulk surrounding the core represent the Sr columns and the less bright columns are the Ti-O columns. The pure O columns in this orientation are not visible, due to the small scattering amplitude of oxygen. The center of the dislocation core contains five Sr, two Ti-O, and five O-columns. The structure of the dislocation core for this geometry according to *ab initio* calculation[15] is superimposed on the image. Here, the Ti-O columns in the center of the dislocation core are composed of two fully occupied Ti columns with alternating oxygen vacancies.

The two core-loss edges of $SrTiO_3$ that are accessible by EELS are the Ti-$L_{3,2}$ edges and the O-*K* edge. The spectra obtained from the bulk, the grain boundary dislocation core, and the material in between the cores are shown in Figs. 3(a) and 3(b). The Ti-*L* edges from the bulk exhibit the splitting of the individual *L* edges, which is attributed to the crystal field. The $3e_g$ peak of the Ti-L_3 edge is at (462.0 ± 0.5) eV, whereas the $3e_g$-peak of the Ti-L_2 edge is at (467.5 ± 0.5) eV. The O-*K* edge from the bulk contains four distinct peaks in the near edge fine structure, and the onset is located at (532.0 ± 0.5) eV. All the spectra presented in this paper are the sum of 14 individual spectra, acquired for 3*s* each at the same position in the sample and added together to improve the signal-to-noise ratio. They are background subtracted and the intensities are normalized to the continuum 40 eV before the O-*K* edge onset. All the energy scales are normalized to the edge-onset of the O-*K* edge at 532 eV to avoid lateral shifts in the spectra due to fluctuations in the incoming electron energy.

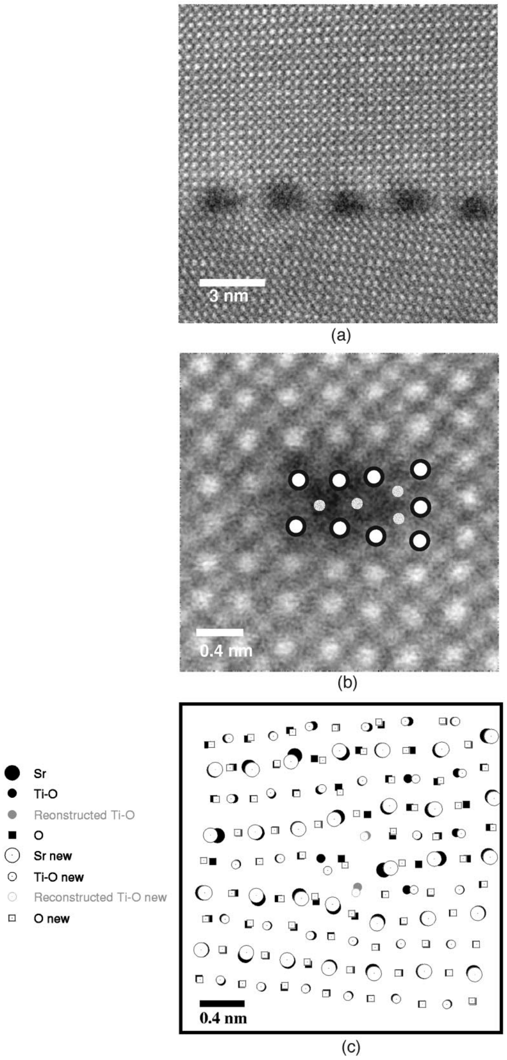

FIG. 2. (a) *Z*-contrast image of a 8° [001] tilt grain boundary in $SrTiO_3$. (b) Higher magnification image of one individual dislocation core. The proposed dislocation core structure is superimposed on the original micrograph. (c) Original structure extracted from (b) and the resulting structure from the DVLS calculations.

The spectrum from the center of the dislocation core [Fig. 3(b)] exhibits four main differences in comparison to the bulk spectrum.

(1) The intensity of the Ti-*L* edge is 21% higher in the grain boundary core than in the bulk, indicating a higher Ti concentration in the core.

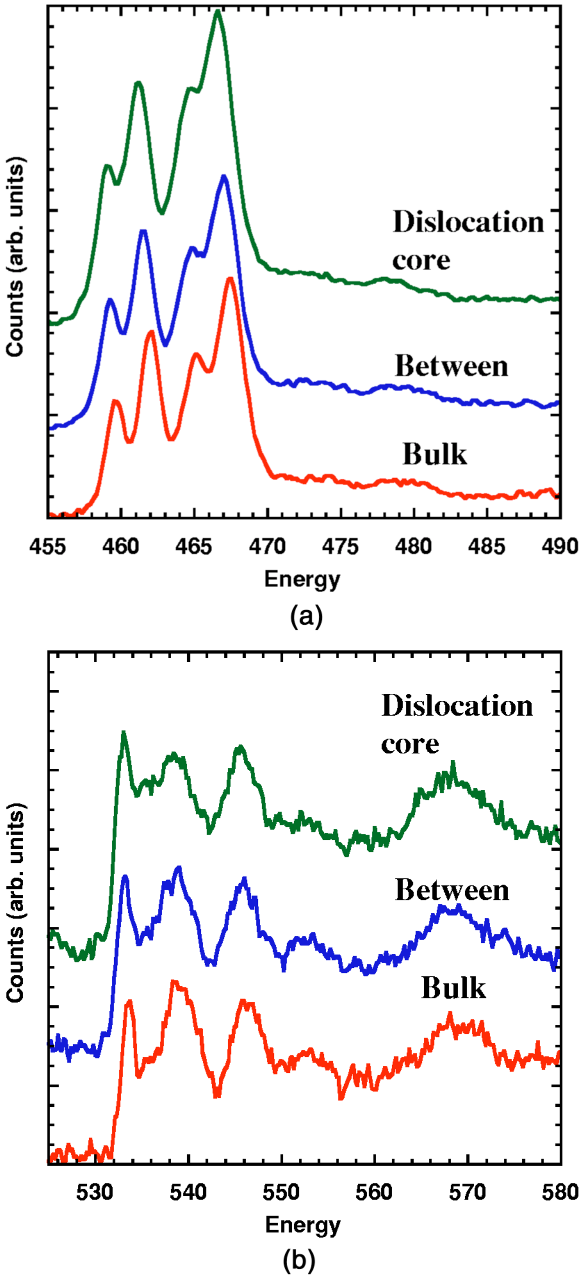

FIG. 3. (a) Ti-L edge from the bulk, the dislocation core center, and the area between the dislocation cores. (b) O-*K* edge of the same areas. The spectra represent a sum of 7–14 individual spectra, acquired with 3*s* acquisition time.

(2) The Ti-*L* edge is shifted by (0.8 ± 0.5) eV shifted toward lower energy-losses, indicating a lower Ti valence in the dislocation core.

(3) The Ti-*L* edge fine structure, namely, the $2t_{2g}$ peaks, is suppressed in height, resembling a mixed T^{3+} and Ti^{4+} valence state.[23]

(4) The relative peak intensity for the four peaks in the O-*K* edge fine structure is different in the grain boundary core, that is, the first peak shows an increased intensity, whereas the second and fourth peaks show a significant reduction in intensity.

The spectra from the material in between the individual dislocation cores exhibit features that are very similar to the bulk. Although a slight shift in the Ti-*L* edge and a minor change in the fine structure can be seen in this region, these features lie within the experimental error and cannot be clearly distinguished from the bulk.

To determine the complete three-dimensional structure of the grain boundary without having to resort to complex theoretical calculations, we need to verify that the number of atoms and the approximate structure of the boundary are correct. One simple means to do so is the combined distance least-squares and bond-valence sum analysis of the *Z*-contrast image. This distance-valence least-squares analysis (DVLS) is based on a concept that was originally proposed by Pauling.[24] In Pauling's rules for crystal chemistry, it is assumed that the formal valence state of a given atom is composed of contributions from all the nearest neighbors. Additionally, the contribution to the valence from each of the neighbors should be as uniform as possible, i.e., the contributions to the formal valence state of an atom are shared equally between the nearest neighbors. These ideas have been further developed by Altermatt and Brown.[25,26] In a systematic study of crystal structures, they find that the contribution of a single bond to the formal valence state of the atoms involved follows the empirical relationship

$$S=e^{(r_{ij}-r_0)/B}, \tag{1}$$

where r_{ij} is the bond length, r_0 is the equilibrium value for each atom pair, and B is a constant $(B=0.37)$. While this relationship is determined only for perfect crystals, there is every reason to believe that the same basic principles will apply to grain boundaries.[27] Although such a minimization is by no means as accurate as *ab initio* calculations, a benefit of this simple approach is that it requires minimal computation, and within the errors, it can verify that the number of atoms and their positions in the structure are physically reasonable.

The starting structure for the DVLS minimization is extracted from the *Z*-contrast image shown in Figs. 2(b) and 2(c). The atomic species are identified using the image intensities in the bulk of the grain (>1.2 nm from the dislocation core) and extended into the immediate core area. Therefore, the intensities in the *Z*-contrast image are not directly interpreted from the grain boundary to avoid problems associated with residual coherence effects in the image. Immediately obvious from the image are positions where two Ti-O columns are very close together, where like ion repulsion should preclude such a structure. However, we know that the *Z*-contrast image provides mostly incoherent image information and atomic columns must therefore exist in each of the positions. Kim *et al.*[15] have previously analyzed such dislocation core structures using *ab-initio* calculations and have shown that two full columns of Ti, but only half columns of O (i.e., a 2×1 reconstruction on the oxygen sub-lattice) are energetically favorable for such a structure. The structure on which the DVLS analysis is performed therefore includes these reconstructed atomic columns as shown in Fig. 2(c).

To perform the minimization, a formal valence state of the elements involved is assumed. Oxygen (2^-) and strontium

(2^+) are assumed to only exist in one valence state. For titanium, we assumed a formal valence state of 4^+ in the bulk and 3^+ in the dislocation core center. The chemical shift and the changes in the Ti-*L* edge fine structure justify such an assumption. The oxygen positions are not known from the *Z*-contrast image, but as the O-*K* edge fine-structure does not change radically, the coordination should be nearly the same as in the bulk. The resulting structure of the DVLS minimization is shown in Fig. 2(c), where the initial structure is indicated by the solid circles and squares, whereas the minimized atom positions are shown by their hollow counterparts. It can be seen from the image that after the minimization process was completed the average shift in the atomic position was 0.1 Å for the determined bulk and 0.2 Å for the dislocation core; the average Ti valence in the dislocation core is (3.3 ± 0.2). With the minimized structure at hand we are now able to use the three-dimensional structure from any position in the boundary as a starting model to simulate the energy-loss spectrum with multiple-scattering analysis.

The multiple-scattering (MS) simulations for the EELS spectra are performed using the FEFF8 codes.[28] These simulations are based on a self-consistent real-space multiple-scattering approach that calculates the x-ray absorption near-edge structure of the desired core-loss edge using *ab initio* codes. FEFF8 can be used in arbitrary aperiodic or periodic systems, typically containing more than 100 atoms, while including full multiple scattering from atoms within a well-defined cluster. Higher-order multiple-scattering contributions from atoms outside this cluster are also taken into consideration. The near-edge fine structure of the simulated spectra converges for cluster sizes of 84 atoms, and all the subsequent MS simulations are performed on clusters of this size.

Figure 4(a) shows both the experimental and the simulated bulk spectra of the O-*K* edge. In the bulk, all the peak positions as well as the peak intensities are reproduced by the simulations, which have an energy resolution of 0.8 eV, compared to the 1.0 eV experimental energy resolution. For the multiple-scattering calculations of the dislocation core [Fig. 4(b)], we calculated the individual spectra for the two reconstructed O columns in the center of the dislocation core and all other complete O columns that are within a 2 Å radius from the center of the dislocation core. These oxygen columns, surrounding the dislocation core, have to be included in the simulations due to diameter of the electron beam (i.e., probe size ~2 Å). The comparison between the experiment and the simulations [Fig. 4(b)] exhibits that the experimental peak position and also the relative peak intensities are reproduced well in the theoretical spectrum. The individual peak intensities and the peak separation seem to be smaller in the simulations, which could be attributed to residual bulklike contribution in the experimental spectra due to specimen drift, or to the unknown ratio of the individual O-column contribution to the final dislocation core spectrum. Nevertheless, these results confirm the minimized structure and therefore verify the three-dimensional structure of the grain boundary in $SrTiO_3$.

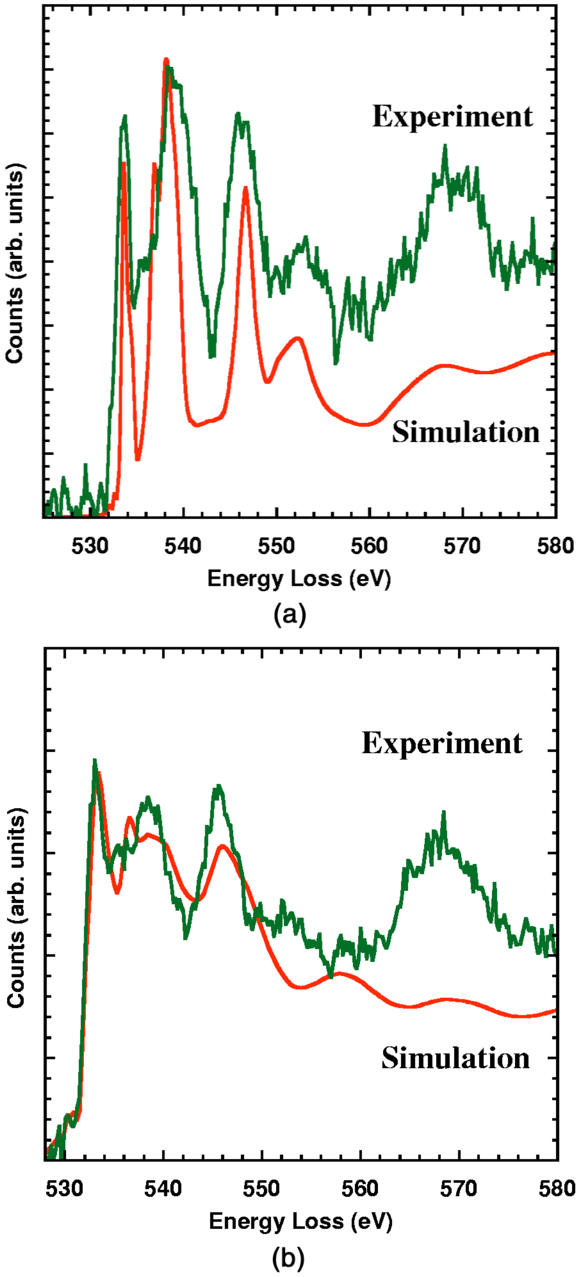

FIG. 4. Comparison of the experimental O-*K* edge with the MS-simulation results (a) from the bulk and (b) from the center of the dislocation core.

58° [001] tilt grain boundary

In this section experimental data from a 58° [001] tilt grain boundary in $SrTiO_3$ will be presented. Figure 5(a) shows a *Z*-contrast image of the grain boundary obtained where the brighter spots represent the Sr columns and the darker spots are the Ti-O columns. This symmetric grain boundary exhibits the same structural units as described above. Half columns of strontium form the center of the grain boundary dislocation cores.[29,30] The spacing between the individual dislocation cores was measured at $d^{58°}=(6.4\pm0.7)$ Å. In this image the interface appears darker than the surrounding bulk, due to the lower density of material in the

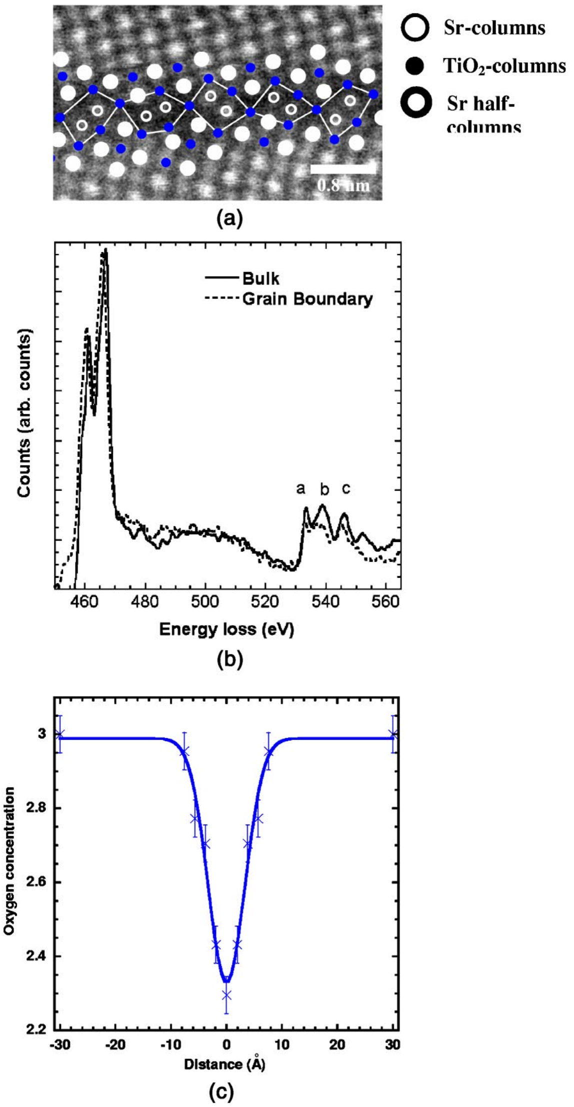

FIG. 5. *Z*-contrast image of a 58° [001] tilt grain boundary in $SrTiO_3$, indicating the half-occupied Sr columns in the center of the dislocation cores. (b) EELS from the bulk and the grain boundary, showing the lower oxygen concentration in the grain boundary; (c) profile of the oxygen concentration perpendicular to the grain boundary plane as measured by column-by-column EELS.

grain boundary and, additionally, to the strain that is exerted from the dislocation cores. Figure 5(b) displays the sum of 15 background-subtracted and multiple-scattering deconvoluted spectra, which show the differences between the bulk and the grain boundary spectra. The spectra are normalized to the continuum interval 30 eV before the onset of the oxygen *K* edge (532 eV). The most obvious change is the lower intensity of the boundary oxygen *K*-edge spectrum. Additionally there is a small change in the fine-structure of the oxygen *K* edge, with peak *C* being much more visible than peaks *A* and *B* in the boundary. This reduction of peaks *A* and *B* and fewer counts under the oxygen *K* edge, suggest a destruction of long-range order and the presence of excess oxygen vacancies at the $SrTiO_3$ grain boundary.[27] Additional evidence for the presence of oxygen vacancies is provided by a shift in the Ti-*L* edge of (1.4 ± 0.6) eV down in energy. The integrated Ti:O intensity ratio is also increased by 25% at the grain boundary, again suggesting oxygen vacancies. In addition to these spectra a set of EELS from the dislocation-core center and four adjacent columns perpendicular to the interface was taken. At each position up to 14 spectra were summed up for an improved signal-to-noise ratio. The bulk spectra are obtained from an area more than 20 nm away from the interface. From the acquired core-loss spectra across the interface, it is now possible to measure the oxygen content in the $SrTiO_3$ material as a function of distance from the boundary by extracting the Ti:O ratio at each location. The difference of this ratio with respect to the bulk value as a function of distance from the interface gives the oxygen concentration profile [Fig. 5(c)]. The oxygen concentration profile resembles the shape of a Gaussian function $3-[O]e^{-x^2/R^2}$, where $[O]=0.7\pm 0.1$ and $R=(4.7\pm 0.7)$ Å are two parameters characterizing the charge distribution, and x is the distance from the grain boundary plane.

DISCUSSION

We have shown in this paper that the dislocation cores in a $SrTiO_3$ [001] 8° tilt grain boundary are Ti rich. The experimental spectra show a 21% increase in the Ti:O intensity ratio at the center of the dislocation core, as previously suggested[15] and independently confirmed by our theoretical modeling. Further, the chemical shift in the Ti-*L* edge as well as the changes in the fine structure[23] infer that the Ti valence in the core is reduced. Sankararman and Perry[31] used standard Ti_xO_y samples to calibrate the chemical shift as a function of the nominal Ti valence. Based on these measurements, a chemical shift of 0.8 eV corresponds to a Ti valence of (3.6 ± 0.2). This value is close to the results of the DVLS calculations, which predict an average Ti valence of (3.3 ± 0.2). The dislocation core charges can now be calculated, by using a fixed oxygen oxidation state of 2^- and the reduced Ti valence. Taking this into consideration, we find a net charge per dislocation of (0.7 ± 0.1) excess electrons per structural unit. The assumption about the constant oxygen valence is justified by bulk measurements,[12] theoretical modeling,[15] and the DVLS calculation presented here, which exhibit an average oxygen valence of $\sim 2^-$.

The results from the $SrTiO_3$ [001] 58° tilt grain boundary show that the dislocation cores containing half columns of Sr atoms are depleted of oxygen, exhibiting a 25% increase in the oxygen vacancy concentration. The excess charge carriers created by the oxygen vacancies are partially compensated by the reduction of the Ti valence from $4+$ to $3.3+$. Taking into consideration the overlap of the charge profiles between the dislocation cores, a net charge of (0.5 ± 0.1) e^-/unit cell is found.

In the structural-unit model, the grain boundary for each misorientation angle is considered to be composed of unique sequence of such units, and the distance between the dislocations cores is only determined by the misorientation angle. Hence, we can assume that the charge profile perpendicular to the interface in the 8° [001] grain boundary exhibits a shape similar to that of the 58° misorientation angle, with a grain boundary width [full width at half maximum (FWHM)] of (7.8 ± 1.4) Å.

We will calculate the excess charge density in the grain boundary now based on two different models for each misorientation angle. In the first model, the charge density in the interface is composed of a series of charges located at the center of the dislocation core. Depending on the misorientation angle, and therefore also the spacing between the individual dislocations, the charge densities will overlap or be completely separated [see Fig. 1(a)]. The density of states is calculated by integrating the charge distribution around a core:

$$S_D = \frac{\pi R^2 \rho_0}{e}, \tag{2}$$

where ρ_0 can be taken directly from the experiment. For the 8° grain boundary, with $\rho_0^{8^\circ} = (0.7\pm 0.1)\ e^-/\mathrm{u.c}$, $S_D^{8^\circ} = 7.7\times 10^9\ \mathrm{m}^{-1}$, while for the 58° interface $[\rho_0^{58^\circ} = (0.5\pm 0.1)]$ $S_D^{58^\circ} = 5.6\times 10^9\ \mathrm{m}^{-1}$. Please note that this lower density of states in the 58° grain boundary is not contradictory to the commonly observed higher potential drop at the interface, since $S_D^{58^\circ}$ reflects only a single dislocation core and the spacing between such cores is very small.

The second model describes the excess interfacial charges as a 2D-charge distribution S_{GB}. Now, the charge distribution per dislocation core S_D is simply averaged over the dislocation spacing d in the grain boundary plain, so that

$$S_{GB} = \frac{S_D}{d} = \frac{\pi R^2 \rho_0}{de}. \tag{3}$$

For the 8° grain boundary, with $d^{8^\circ} = (26.8\pm 0.7)$ Å, $S_{GB}^{8^\circ} = 2.9\times 10^{18}\ \mathrm{m}^{-2}$, while for the 58° interface with $d^{58^\circ} = (6.4\pm 0.7)$ Å, $S_{GB}^{58^\circ} = 8.8\times 10^{18}\ \mathrm{m}^{-2}$.

Thomas-Fermi screening model

These negative excess charge distributions will attract positive charge carriers in the vicinity of the interface, thereby causing a screening effect. To find the form and extent of the screened electrostatic potential $\phi(\mathbf{r})$ induced by a generic charge distribution $\rho(\mathbf{r})$, we have to solve the Thomas-Fermi screening equation:[32]

$$\nabla^2 \phi(\mathbf{r}) - \frac{\phi(\mathbf{r})}{l_s^2} = -\frac{1}{\varepsilon\varepsilon_0}\rho(\mathbf{r}), \tag{4}$$

where l_s is the screening length, ε and ε_0 are the relative dielectric constant and the permittivity of vacuum, respectively.

Performing a 3D Fourier transform into **k** space, Eq. (4) now reads

$$\phi(\mathbf{k})(k^2 + k_0^2) = \frac{1}{\varepsilon\varepsilon_0}\rho(\mathbf{k}), \tag{5}$$

where $k_0 = 1/l_s$. Equation (5) shows that the solution for the potential can be easily obtained once the Fourier transform of the charge distribution is known.

For the grain boundaries considered in this study, we obtain the following solutions:

$$\phi_{1D}(r) = \frac{S_D e}{2\pi\varepsilon\varepsilon_0}\int_0^\infty \frac{k\,dk}{k^2 + k_0^2} J_0(kr) e^{-1/4k^2R^2} \tag{6}$$

for the core charge distributions and

$$\phi_{2D}(x) = \frac{S_{GB} e}{2\varepsilon\varepsilon_0 k_0} e^{-k_0|x|} \tag{7}$$

for the 2D sheet of charges located in the grain boundary plain.

The integral in Eq. (6) cannot be easily expressed in terms of elementary function, therefore we have to evaluate it numerically. However, as we are interested mainly in the potential drop at the origin, we can give an analytical expression for $\phi_{1D}(0)$:

$$\phi_{1D}(0) = \frac{\pi\rho_0 R^2}{2\varepsilon\varepsilon_0} e^{(1/4)k_0^2R^2} \sum_{-\infty}^{\infty} \frac{\mathrm{erfc}\left(\frac{R}{2d}K_j\right)}{K_j}, \tag{8}$$

where $K_j = \sqrt{(2\pi j)^2 + (dk_0)^2}$ and $\mathrm{erfc}(z)$ is the complementary error function.

The screening length l_s for $\mathrm{SrTiO_3}$ is estimated using the Thomas-Fermi model.

In this limit, the screening length can be found to be[33]

$$l_{TF} = \sqrt{\frac{\pi\varepsilon a_0}{4(3\pi^2 p_0)^{1/3}}}, \tag{9}$$

where $a_0 = 0.53$ Å is the Bohr radius and p_0 is the number of charge carriers. Chang *et al.*[34] reported that nominally undoped $\mathrm{SrTiO_3}$ typically contains 100–200 at. ppm of acceptor impurities and we will therefore assume a density of carriers (holes) in the bulk of $p_0 = 1.7\times 10^{25}\ \mathrm{m}^{-3}$. The value of the relative dielectric constant was assumed to be that of the bulk at $\varepsilon = 332$. In this case, the screening length of nominally undoped $\mathrm{SrTiO_3}$ is $l_{TF} = 4.2$ nm.

Since the screening length is comparable to the spacing between the dislocation cores, the resulting grain boundary potential is a superposition of the individual dislocation core potentials for all misorientation angles presented in this paper. The potential barrier height at the center of the grain boundary plane can now be found using Eq. (8) to be $\phi_{1D}^{8^\circ}(0) = -(0.3\pm 0.1)$ V. Using the same picture, the potential barrier height for the 58° grain boundary is $\phi_{1D}^{58^\circ}(0) = -(0.9\pm 0.1)$ V. Combining Eqs. (3) and (7) we find that $\phi_{2D}^{8^\circ}(0) = -(0.3\pm 0.1)$ V and $\phi_{2D}^{58^\circ}(0) = -(1.0\pm 0.1)$ V for the 2D sheet of charges located in the grain boundary plane. Figure 6 shows 3D plots of the interfacial potential in the Thomas-Fermi approach, using both charge distributions for the 8° and 58° grain boundary.

Since the valence band in undoped $\mathrm{SrTiO_3}$ is roughly 3–4 eV wide,[35] and the value of p_0 together with the dimensionality of the material (3D) position the Fermi level around 11 meV from the valence-band top edge, we can safely assume

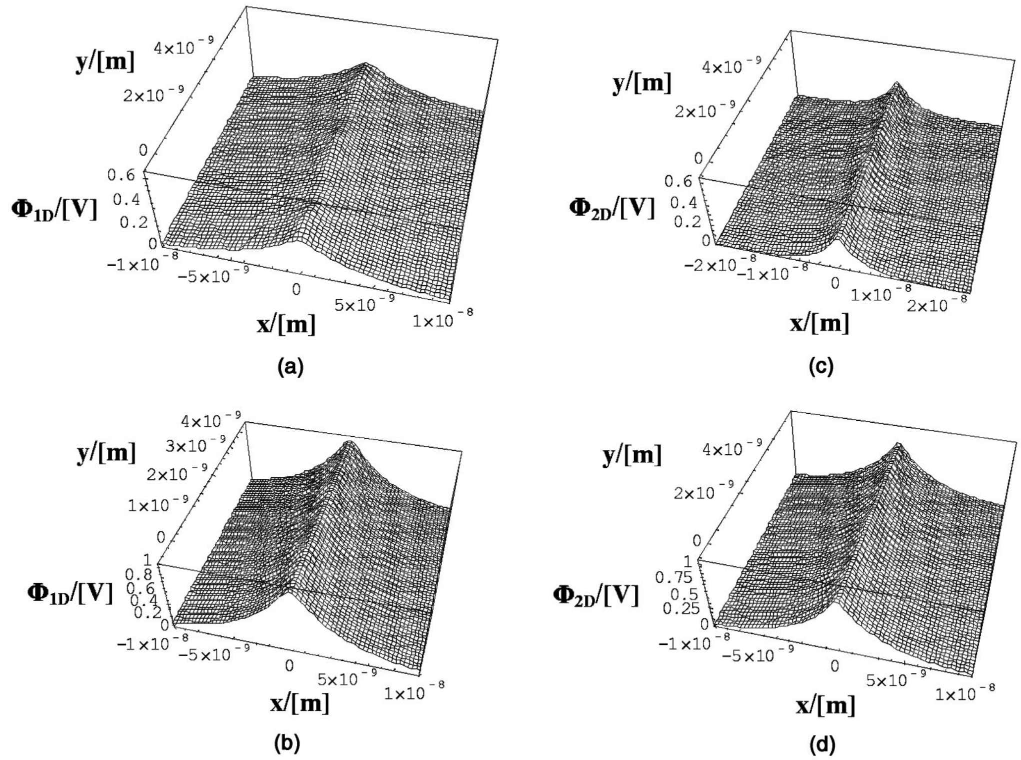

FIG. 6. Plot of the grain boundary potential in the Thomas-Fermi screening model: 3D plot for (a) 8° misorientation angle and (b) 58° misorientation angle using the charge distribution from the sum of individual core charges; (c) 8° misorientation angle and (d) 58° misorientation angle using the 2D wall of charges.

that the Thomas-Fermi formalism is applicable for negative potentials of the order of 0.5 eV.

Schottky barrier model

The classical model of a back-to-back Schottky barrier adopts the picture of a continuous wall of negative charges located in the grain boundary plane. In this model, there are negative grain boundary interface states and localized holes giving rise to an electrostatic repulsion of the mobile charge carriers at both sides of the grain boundary plane. Sutton and Balluffi[36] have shown that by solving the Poisson equation for a two-dimensional charge distribution in the grain boundary plane, the grain boundary potential is given by

$$\phi_{SM}(x)=\frac{eSL_D}{4\varepsilon\varepsilon_0}\left(1-\frac{|x|}{L_D}\right)^2, \tag{10}$$

where S is the density of grain boundary states and $L_D=S/2L_D$ is the depletion layer width. This treatment of the grain boundary potential is only valid if the induced grain boundary charges and the bulk charge carriers are of equal signs (i.e., both are either electrons or holes), since only in this case a depletion layer due to the electrostatic repulsion occurs. In our case, where the grain boundary core charges are negative, but the bulk charge carriers are holes, we have to adopt a different model with an accumulation rather than a depletion layer. Chazalviel[8] and Tredgold[37] have shown that the grain boundary potential in this case can be written as

$$\phi_{SC}(x)=\frac{2k_BT}{e}\ln\left|\cos\left(-\frac{|x|-L_{\mathrm{SC}}}{l_{\mathrm{D}}\sqrt{2}}\right)\right| \tag{11}$$

with $L_{SC}=l_D\sqrt{2}\cos^{-1}[e^{e\phi_{SC}(0)/2k_BT}]$ and

$$S_{GB}^2=2e\varepsilon\varepsilon_0p_0[e\phi_{SC}(0)+k_BT(e^{(-e\phi_{SC}(0)/k_BT)}-1)], \tag{12}$$

where l_D is the Debye screening length. The Debye-Hueckel limit describes the classical treatment of mobile charges in solution. For a low carrier density, the Debye screening length can be expressed as[8]

$$l_D=\sqrt{\frac{\varepsilon\varepsilon_0k_BT}{e^2p_0}}, \tag{13}$$

where k_B is the Boltzmann constant, T the temperature, and p_0 is the number of charge carriers. The screening length for undoped $SrTiO_3$, using the Debye model is then $l_D=3.1$ nm.

Since Eq. (12) cannot be solved analytically, we have to evaluate this equation numerically and find for the 8° grain boundary a potential drop of $\phi_{SC}^{8°}(0)=-(0.2\pm0.1)$ eV. For the 58° grain boundary we find a grain boundary potential of $\phi_{SC}^{58°}(0)=-(0.2\pm0.1)$ eV. These values are significantly smaller than potentials calculated using the Thomas-Fermi approach (see Table I) and do not account for the angular

TABLE I. Grain boundary potential for the different charge distributions using the Thomas-Fermi screening and the Schottky model approach.

Misorientation angle	S_D (V)	S_{GB} (V)	S_a (V)
8°[001]	−0.3	−0.3	−0.2
58°[001]	−0.9	−1.0	−0.2

dependence of the grain boundary potential. The resulting grain boundary profiles for the Schottky model [Figs. 7(a) and 7(b)] show that the potential width for the classical model is also significantly smaller than for the Thomas-Fermi model. This will influence the overall transport properties across the homo-interface.

This difference derives mainly from the assumption underlying the classical Schottky model of a constant accumulation of all the available carriers, which results in underestimating the region affected by the screening. The Thomas-Fermi picture, on the other hand, takes into account better the distribution of the induced charge, which results in a more accurate description of the grain boundary. Certainly, this strongly depends on the band structure of the material. This means that before choosing the appropriate model for the interpretation of the grain boundary potential, it is necessary to have at least some qualitative information about the band structure and the position of the Fermi level in the material. Nevertheless, the Thomas-Fermi screening picture is a more accurate description of the underlying physics in perovskite oxides than the Schottky model.

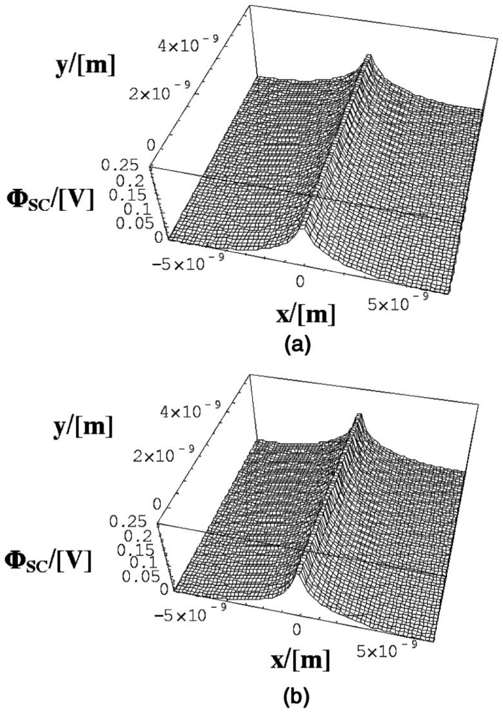

FIG. 7. Plot of the grain boundary potential in the Schottky semiconductor model: (a) 3D plot of the 8° misorientation angle and (b) 3D plot of the 58° misorientation angle.

We have shown that both, the Thomas-Fermi and the Schottky model approaches for calculating the grain boundary potential in $SrTiO_3$ result in a similar interfacial potential shapes, although the potential drop in the grain plane differs greatly for the two models. Nevertheless, the values obtained from the Thomas-Fermi approach are in agreement with the grain boundary potentials found in the literature. The reported results range from 0.3 V for an undoped 24° [001] tilt grain boundary to (0.9±0.3) V for 0.2% Fe doped,[38] 1.2 V for a 0.2% Ni doped polycrystalline samples,[12] and 1.3 V for 0.16% Ni doped grain boundaries.[39] The effect of the acceptor doping will effectively lower the grain boundary potential. Please note that for donor doped $SrTiO_3$ the classical semiconductor approach (Eq. 10) has to be applied, which will result in a large depletion layer depending on the bulk donor dopant concentration.

CONCLUSIONS

In this paper, we have developed an atomic-scale model for the grain boundary potential in cubic perovskite oxides and have shown its validity for both, high- and low-angle tilt grain boundaries. In the case of low-angle grain boundaries, where the individual dislocation cores do not overlap (i.e., spacing is larger than the screening length), we have shown that the Thomas-Fermi screening model describes better the interfacial potential. The classical Schottky model largely underestimates the potential for such low-angle grain boundaries, in particular for materials with high charge carrier concentrations and small screening length. In high-angle tilt grain boundaries, the Schottky barrier model is frequently used to calculate the interfacial potentials. We showed that for acceptor doped $SrTiO_3$ this model is not suitable and that the model of a grain boundary accumulation layer has to be used. This model does not seem to be able to account for the angular dependence of the grain boundary potential within the error bars, since it results in identical potentials for both the high- and low-angle grain boundaries. Further, the Thomas-Fermi screening equation described this situation more accurately, and large differences in both the potential height and width between the Schottky and the Thomas-Fermi models were noted.

For perovskite oxides, where the charge carrier concentration is significantly higher than in the material discussed in this paper, the classical Schottky model using a 2D sheet of charges will fail in determining the potential for low-angle tilt grain boundaries. Since the 1D charge distribution model results in the most consistent interfacial potential for $SrTiO_3$, we will adopt this model in the future to describe those cubic perovskite oxide tilt grain boundary systems, where the interfacial potential is small compared to the band width and the Fermi level is not very close to the top or bottom edge of the band. In this case, the Thomas-Fermi screening model can be easily applied to a large range of misorientation angles in tilt grain boundaries, where only the dislocation core spacing and the density of states at the center of the core is changing as a function of misorientation angle.

In the future, we will develop an atomic-scale charge transport model, based on tunneling of the charge carriers through the interfacial potential. The comparison of this model with conductivity measurements across such homointerfaces will provide a direct test for the proposed model and will lead to a more complete understanding of the atomic-scale structure-property relationship at grain boundaries in cubic perovskite oxides.

ACKNOWLEDGMENTS

This work was supported by the U.S. Department of Energy, Division of Materials Sciences, Office of Basic Energy Science, under Contract Nos. DE-AC02-98CH10886 and DOE FG02 96ER45610. The experimental results were obtained in parts on the JEOL 2010F operated by the Research Resources Center at UIC and funded by NSF.

---

*Electronic address: klie@bnl.gov

[1] J.G. Bednorz and K.A. Muller, Phys. Rev. Lett. **52**, 2289 (1984).

[2] M. Carona, Phys. Rev. A **140**, A651 (1965).

[3] D. Dimos, P. Chaudhari, and J. Mannhart, Phys. Rev. B **41**, 4038 (1990).

[4] Y. M. Chiang, D. Birnie, and W. D. Kingery, *Physical Ceramics* (MIT Press, Cambridge, 1997).

[5] M.M. McGibbon, N.D. Browning, M.F. Chrisholm, A.J. McGibbon, S.J. Pennycook, V. Ravikumar, and V.P. Dravid, Science **266**, 102 (1994).

[6] N.D. Browning, J.P. Buban, H.O. Moltaji, G. Duscher, S.J. Pennycook, R.P. Rodrigues, K. Johnson, and V.P. Dravid, Appl. Phys. Lett. **74**, 2638 (1999).

[7] K.L. Kliewer and J.S. Koehler, Phys. Rev. **140**, A1226 (1965).

[8] J. N. Chazalviel, *Coulomb Screening by Mobile Charges* (Birkhaeuser Press, Basel, 1999).

[9] I. Denk, J. Claus, and J. Maier, J. Electrochem. Soc. **144**, 3526 (1997).

[10] Y.M. Chiang and T. Takagi, J. Am. Ceram. Soc. **1990**, 3278 (1990).

[11] R. Waser, Solid State Ionics **75**, 89 (1995).

[12] R. Hagenbeck and R. Waser, J. Appl. Phys. **83**, 2083 (1998).

[13] N.D. Browning and S.J. Pennycook, J. Phys. D **29**, 1779 (1996).

[14] M.M. McGibbon, N.D. Browning, A.J. McGibbon, M.F. Chisholm, and S.J. Pennycook, Philos. Mag. A **73**, 625 (1996).

[15] M. Kim, G. Duscher, N.D. Browning, K. Sohlberg, S.T. Pantelides, and S.J. Pennycook, Phys. Rev. Lett. **86**, 4056 (2000).

[16] E.M. James and N.D. Browning, Ultramicroscopy **78**, 125 (1999).

[17] E.M. James, N.D. Browning, A.W. Nicholls, M. Kawasaki, Y. Xin, and S. Stemmer, J. Electron Microsc. **47**, 561 (1998).

[18] P.D. Nellist and S.J. Pennycook, Ultramicroscopy **78**, 111 (1999).

[19] J.M. Cowley, J. Electron Microsc. Tech. **3**, 25 (1986).

[20] R. F. Egerton, *Electron Energy Loss Spectroscopy in the Electron Microscope* (Plenum Press, New York, 1986).

[21] J. Fertig and H. Rose, Optik (Jena) **59**, 407 (1981).

[22] N.D. Browning, M.F. Chrisholm, and S.J. Pennycook, Nature (London) **366**, 143 (1993).

[23] A. Ohtomo, D.A. Muller, J.L. Grazul, and H.Y. Hwang, Nature (London) **419**, 378 (2002).

[24] L.J. Pauling, J. Am. Ceram. Soc. **51**, 1010 (1929).

[25] D. Altermatt and I.D. Brown, Acta Crystallogr., Sect. B: Struct. Sci. **B41**, 240 (1985).

[26] I.D. Brown and D. Altermatt, Acta Crystallogr., Sect. B: Struct. Sci. **B41**, 244 (1985).

[27] N.D. Browning, H.O. Moltaji, and J.P. Buban, Phys. Rev. B **58**, 8289 (1998).

[28] A.L. Ankudinov, B. Ravel, J.J. Rehr, and S.D. Conradson, Phys. Rev. B **58**, 7565 (1998).

[29] R.F. Klie and N.D. Browning, Appl. Phys. Lett. **77**, 3737 (2000).

[30] R.F. Klie and N.D. Browning, Defect Diffus. Forum **a203-a207**, 31 (2002).

[31] M. Sankararaman and D. Perry, J. Mater. Sci. **27**, 2731 (1992).

[32] A. Gurevich and E.A. Pashitskii, Phys. Rev. B **57**, 13 878 (1998).

[33] H. Ibach and H. Lueth, *Solid State Physics* (Springer, Berlin, 1996).

[34] E.K. Chang, A. Mehta, and D.M. Smyth, J. Electrochem. Soc. **134**, C473 (1987).

[35] S.D. Mo, W.Y. Ching, M.F. Chisholm, and G. Duscher, Phys. Rev. B **60**, 2416 (1999).

[36] A. P. Sutton and R. W. Balluffi, *Interfaces in Crystalline Materials* (Oxford Science Publications, Oxford, 1995).

[37] R. H. Tredgold, *Space Charge Conduction in Solids* (Elsevier, Amsterdam, 1966).

[38] V. Ravikumar, R.P. Rodrigues, and V.P. Dravid, J. Phys. D **29**, 1799 (1996).

[39] P.C. McIntyre, J. Am. Ceram. Soc. **83**, 1129 (2000).